

# A SHELL OF THERMAL X-RAY EMISSION SURROUNDING THE YOUNG CRAB-LIKE REMNANT 3C58

E. V. GOTTHELF, D. J. HELFAND, & L. NEWBURGH

Columbia Astrophysics Laboratory, Columbia University, 550 West 120<sup>th</sup> Street, New York, NY 10027, USA; eric@astro.columbia.edu  
*Draft version January 31, 2018*

## ABSTRACT

Deep X-ray imaging spectroscopy of the bright pulsar wind nebula 3C58 confirms the existence of an embedded thermal X-ray shell surrounding the pulsar PSR J0205+6449. Radially resolved spectra obtained with the *XMM*-Newton telescope are well-characterized by a power-law model with the addition of a soft thermal emission component in varying proportions. These fits reproduce the well-studied increase in the spectral index with radius attributed to synchrotron burn-off of high energy electrons. Most interestingly, a radially resolved thermal component is shown to map out a shell-like structure  $\approx 6'$  in diameter. The presence of a strong emission line corresponding to the Ne IX He-like transition requires an overabundance of  $\sim 3 \times [\text{Ne}/\text{Ne}_{\odot}]$  in the Raymond-Smith plasma model. The best-fit temperature  $kT \sim 0.23$  keV is essentially independent of radius for the derived column density of  $N_{\text{H}} = (4.2 \pm 0.1) \times 10^{21}$  cm<sup>-2</sup>. Our result suggests that thermal shells can be obscured in the early evolution of a supernova remnant by non-thermal pulsar wind nebulae emission; the luminosity of the 3C58 shell is more than an order of magnitude below the upper limit on a similar shell in the Crab Nebula. We find the shell centroid to be offset from the pulsar location. If this neutron star has a velocity similar to that of the Crab pulsar, we derive an age of 3700 yr and a velocity vector aligned with the long axis of the PWN. The shell parameters and pulsar offset add to the accumulating evidence that 3C58 is not the remnant of the supernova of CE 1181.

*Subject headings:* stars: individual (PSR J0205+6449, 3C58) — ISM: supernova remnant — stars: neutron — X-rays: stars — pulsars: general

## 1. INTRODUCTION

A long standing puzzle in supernova physics is the apparent lack of an associated thermal shell surrounding a few young pulsars with bright relativistic wind-powered nebulae (PWNe). Though relatively rare, with fewer than ten examples known, the lack of a supernova remnant shell is at odds with our current understanding of supernova evolution and neutron star formation. The canonical examples, the Crab and 3C58, are both putative historical remnants less than 1000 yrs old. To date, no evidence has been found for thermal emission associated with the Crab Nebula pulsar despite repeated searches (Seward et al. 2006 and references therein). However, recent *XMM*-Newton and *Chandra* observations have identified thermal emission within the 3C58 remnant (Bocchino et al. 2001; Slane et al. 2004). The availability of a large quantity of XMM archival data on this source derived from calibration observations allows us to construct very sensitive images and spectra to explore the evidence for a surrounding SNR shell with unprecedented sensitivity.

The morphology of 3C58 is well-documented in both the X-ray and radio bands (Slane et al. 2004 and Bietenholz et al. 2006 and references therein). It is center-filled with a 66 msec pulsar near the center, axisymmetric lobes, and an elaborate network of wisps and filaments. Failure to find a radio shell around 3C58 led Reynolds & Aller (1985) to conclude that there is no evidence for its interaction with an external medium. Coupled with the low velocities of the optical filaments (Fesen 1983) compared to the mean expansion velocity required for the remnant to reach its current extent in 820 yr, these results led to suggestions that the remnant was considerably older. Over the past twenty years, further evidence

has accumulated that the remnant's age is inconsistent with an origin in SN1181. The images and spatially resolved spectra we present below add incrementally to the case and provides a testable prediction concerning the pulsar velocity which could support or refute the historical association.

In §2 we describe the available observations and discuss their analysis. Section 3 presents the detailed spatially resolved spectroscopy which allows us to detect clear evidence for a shell of thermal emission, overabundant in Neon, and extending to the edge of the synchrotron nebula; we interpret this result in §4, concluding that the pulsar is offset from the center of the symmetrically expanding shell implying a velocity aligned with the symmetry axis of the remnant. If the pulsar has a Crab-like velocity, this offset provides another argument against an association with SN1181.

## 2. OBSERVATIONS AND RESULTS

### 2.1. The observations

A total of ten pointed observations of 3C58 are available in the public archive of data obtained with the *XMM*-Newton X-ray Observatory (Jansen et al. 2001). Of these, a set of eight pointings, acquired on 2002 September 11 – 13 to perform an in-orbit calibration of the telescope mirror vignetting function (Lumb et al. 2004), used imaging modes with a sufficiently large field-of-view to cover fully the 3C58 nebula. The duration of these observations varied between 17 – 33 ks. An observation log is presented in Table 1.

In this study we concentrate on data obtained with the European Photon Imaging Camera (EPIC; Turner et al. 2001) which consists of three CCD cameras, the EPIC-pn and the two EPIC-MOS imagers. The EPIC-MOS cam-

TABLE 1  
XMM-NEWTON OBSERVATION LOG FOR 3C58<sup>a</sup>

ObsID	Date (UT)	Pointing R.A. (J2000)	pointing Decl. (J2000)	Exposure EPIC-MOS <sup>b</sup> (ks)	Exposure EPIC-pn (ks)
153752201	2002-09-11 04:29:35	2 <sup>h</sup> 4 <sup>m</sup> 43.6 <sup>s</sup>	+64° 51' 13'' 2	36777	15579
153751801	2002-09-11 13:09:58	2 <sup>h</sup> 5 <sup>m</sup> 03.0 <sup>s</sup>	+64° 47' 38'' 6	39561	16328
153752501	2002-09-11 20:03:41	2 <sup>h</sup> 5 <sup>m</sup> 23.4 <sup>s</sup>	+64° 43' 52'' 3	35195	14721
153752401	2002-09-12 03:20:44	2 <sup>h</sup> 6 <sup>m</sup> 32.4 <sup>s</sup>	+64° 48' 06'' 8	26184	...
153752101	2002-09-13 04:22:11	2 <sup>h</sup> 5 <sup>m</sup> 38.0 <sup>s</sup>	+64° 49' 40'' 0	17363	3022
153751701	2002-09-13 10:57:39	2 <sup>h</sup> 5 <sup>m</sup> 18.9 <sup>s</sup>	+64° 53' 23'' 7	13515	6042
153751901	2002-09-13 17:51:22	2 <sup>h</sup> 5 <sup>m</sup> 13.1 <sup>s</sup>	+64° 51' 41'' 8	34114	14569
153752001	2002-09-13 23:45:05	2 <sup>h</sup> 5 <sup>m</sup> 52.6 <sup>s</sup>	+64° 55' 27'' 7	48631	21038

<sup>a</sup>All observations were obtained in pointed imaging mode with the thin transmission window in the focal plane; the EMOS and EPN data were collected with the `PrimeFullWindow` and `PrimeLargeWindow` submodes, respectively

<sup>b</sup>EPIC exposure times are after filtering; the EPIC-MOS exposure times are for the sum of the two MOS cameras.

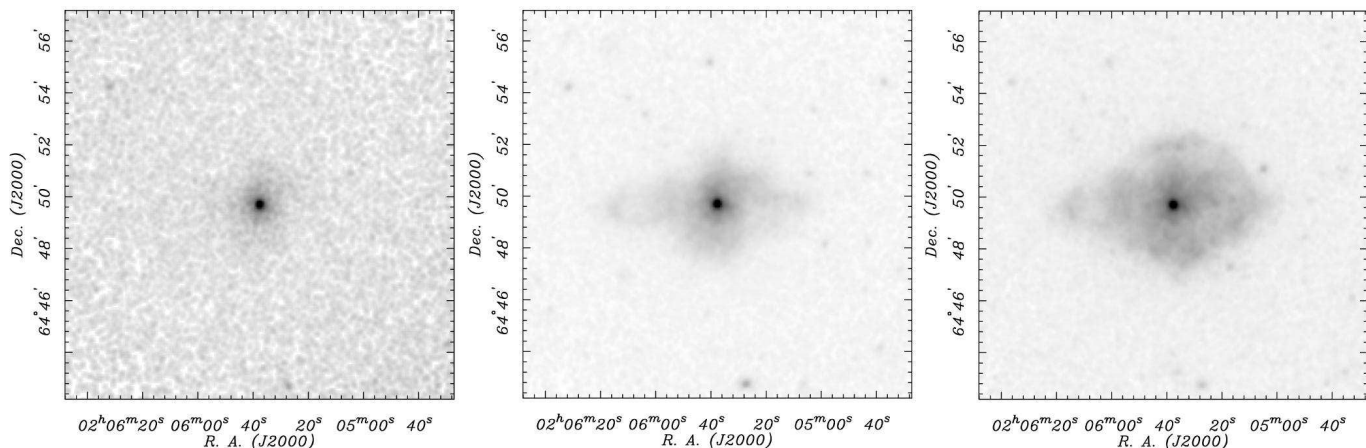


FIG. 1.— Narrow-band X-ray images of 3C58 acquired with the XMM-Newton EPIC cameras. The energy range for these exposure-corrected images separates out three distinct sources of emission, *Left*) the unresolved point-like pulsar emission surrounded by the highest-energy and most intense portion of the PWN (7.0 – 8.0 keV), *Middle*) the pulsar wind nebula in the medium band (2.0 – 3.0 keV), and *Right*) the symmetric shell-like structure in the soft X-ray band (0.5 – 1.0 keV). The pulsar wind nebula image also includes pulsar emission whereas the shell-like structure includes both pulsar and PWN emission components. In each image, the intensity is cropped at 0.6 of the peak intensity and plotted with square-root scaling to highlight the fainter emission.

eras were operated in `FullFrameMode` mode, in which the full 30' diameter field-of-view is read out every 2.7 s. The EPIC-pn was operated in `PrimeLargeWindow` mode, which provides 78 ms time resolution over a 6.9 × 13.5 field-of-view. For all observation, the thin transmission filter was placed in the focal plane. The EPIC instruments are sensitive to X-rays in the 0.2 – 10 keV energy range. The point spread function (PSF) of the mirror modules has a FWHM of 6 – 15'' depending on energy and is fully oversampled by the CCD pixel size in each instrument.

## 2.2. Basic analysis

We analyzed data produced by the standard processing (SAS version 20020507\_1701). The photon event lists were initially filtered for periods of high background, typically flare events corresponding to enhanced solar wind activity. To identify these flares, an iterative clipping method was used to generate the acceptable time intervals using the following method. We first produced a

lightcurve histogram in 100 s steps for the whole instrument and calculated the mean. Intervals with an enhanced count rate  $> 3\sigma$  above the mean were discarded and a new lightcurve was generated. This process was repeated until all points above the converging threshold were removed. The good time intervals (GTIs) thus generated were used to filter the revised event file. A total of  $\sim 343$  ks of good exposure time was acquired from the collective data set; the net exposure times for each instrument are listed in Table 1. Finally, in creating spectra and images, we used the standard SAS screening flags and selected only CCD photons with `PATTERN`  $\leq 4$  and  $\leq 12$  for the EPIC-pn and EPIC-MOS, respectively. Bad CCD pixels and columns were taken into account. We verified that spectra were not affected by photon pile-up in any of the observations.

## 2.3. Spatial analysis

To search for evidence of a faint supernova remnant surrounding the pulsar, we generated exposure-

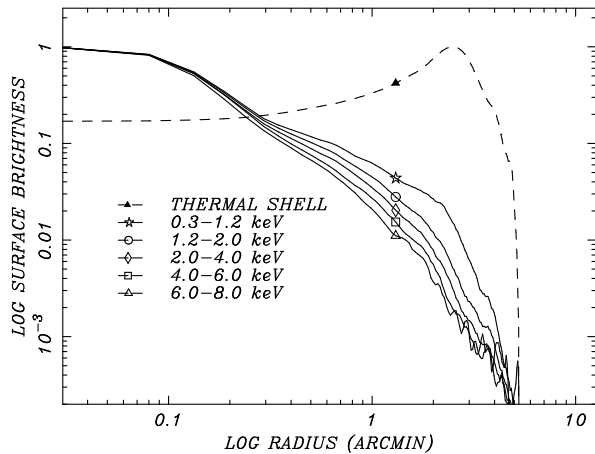


FIG. 2.— Evidence of a thermal shell surrounding the pulsar in 3C58. Normalized background-subtracted radial profiles for five adjacent energy bands from 0.3–8.0 keV obtained with the *XMM-Newton* EPIC CCD detectors. A prominent plateau of emission is seen for the lowest energy profile. A shell-like structure (*dashed-line*) is found for the radial profile of the 0.3–1.2 keV band image after subtracting off the normalized emission in the next highest band.

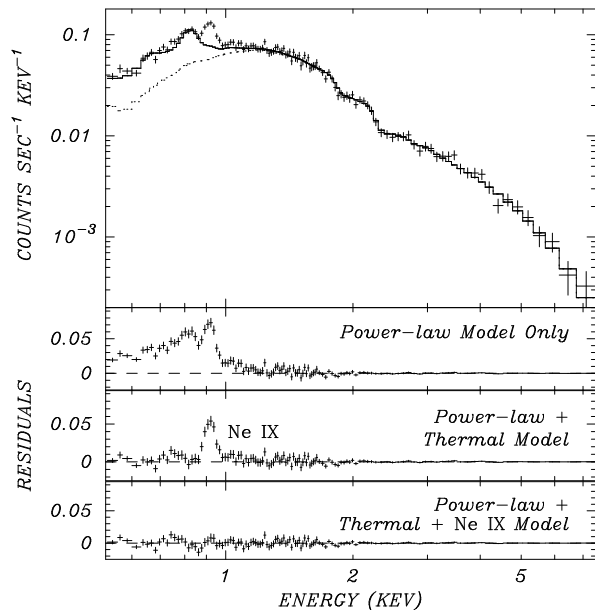


FIG. 3.— Evidence for a thermal component with an overabundance of Neon in 3C58. The solid line in the upper panel represents a best-fit power-law plus Raymond-Smith plasma emission model to the *XMM-Newton* EPIC-MOS spectra (crosses) from annular regions ( $2'0 - 2'5$ ) centered on the pulsar in 3C58. The dotted line shows the power-law component only. Residuals from three different fits are displayed in the lower three panels. The first of these shows a strong excess above the pure power-law model below 1.2 keV. The next panel down shows the residuals from a model that includes an equilibrium thermal R-S plasma with solar abundances. The strong line remaining at  $\sim 0.9$  keV corresponds to a complex of emission lines from Helium-like Neon (Ne IX). The bottom panel shows a fit in which the Neon abundance is three times solar. Model parameters are given in Table 2.

corrected, narrow-band images including data from all three instruments in order to obtain the deepest possible image. Figure 1 compares the image of 3C58 in three energy bands to highlight the three spatial components which are found to make up the composite morphology:

a shell-like nebula (0.5–1.0 keV), the pulsar wind nebula (2.0–3.0 keV), and the point-like pulsar emission (7.0–8.0 keV). This is best illustrated by comparing the radial profiles in the five narrow energy-bands shown in Figure 2. In addition to the steep falloff of flux with radius, it is again clear that the extent of the emission from 3C58 is strongly dependent on energy-band. In particular, the radial profile in the softest energy band displays a large departure from the higher energy profiles between  $2'$  and  $5'$  from the remnant center. Subtracting emission in the 1.2–2.0 keV band from the lowest energy image shows that the soft emission has a radial profile consistent with that of a limb-brightened shell peaking  $\sim 3'$  from the remnant center.

To investigate further the nature of this shell-like emission we generated spectra from concentric annuli  $30''$  wide to search for radial variations. These annuli were centered on the location of the pulsar, the presumed origin of the wind and likely center of any SNR expansion. To estimate the background in each annulus, we collected photons from within a region with  $\sim 3'5 < r < 4'0$ . Although the background is somewhat distant from the inner source regions, the high surface brightness of the source makes background subtraction less important there. We also extracted photons from the eastern “lobe” region, using a circle of radius  $75''$  centered at coordinates RA = 02:06:14.65 and Dec = 64:49:31.9; the background for this region was determined from a pair of apertures straddling the source region to the north and south.

#### 2.4. Spectral analysis

Spectra from each observation were extracted from each annular region using standard channel binning for each instrument, and a set of response matrices were generated for each ring using the standard prescription for diffuse emission. The spectra and response matrices were then summed over all observations for each instrument following the method used in *addaspcaspec*<sup>1</sup>. The two sets of MOS spectra were then combined. Finally, all spectra were grouped into bins containing a minimum of 400 counts and fitted using the *xspec* spectral fitting package.

To fit the summed spectra in each annulus we used the following procedure. In all cases, the EPIC-pn and EPIC-MOS spectra were fitted simultaneously, with the model normalizations allowed to be independent to account for remaining flux calibration differences ( $\lesssim 10\%$ ) between the two instruments (Saxton 2003). The spectra were initially fitted in the 1.5–8.0 keV energy band with a power-law model for the non-thermal emission from the pulsar wind nebula. This model included the effects of interstellar absorption, although this is not an important component in the fitted band. The best-fit values for the power-law index and flux are recorded in Table 2. As illustrated in Figure 3, the spectrum above 1.2 keV is well-characterized by a power-law model. However, at the lower energies, we require additional emission components for the larger annuli. We account for this excess by adding in a Raymond-Smith thermal plasma emission component to the model and extending the fitting range

<sup>1</sup> *addaspcaspec* is part of the FTOOLS software package available at [heasarc.gsfc.nasa.gov/docs/software.html](http://heasarc.gsfc.nasa.gov/docs/software.html)

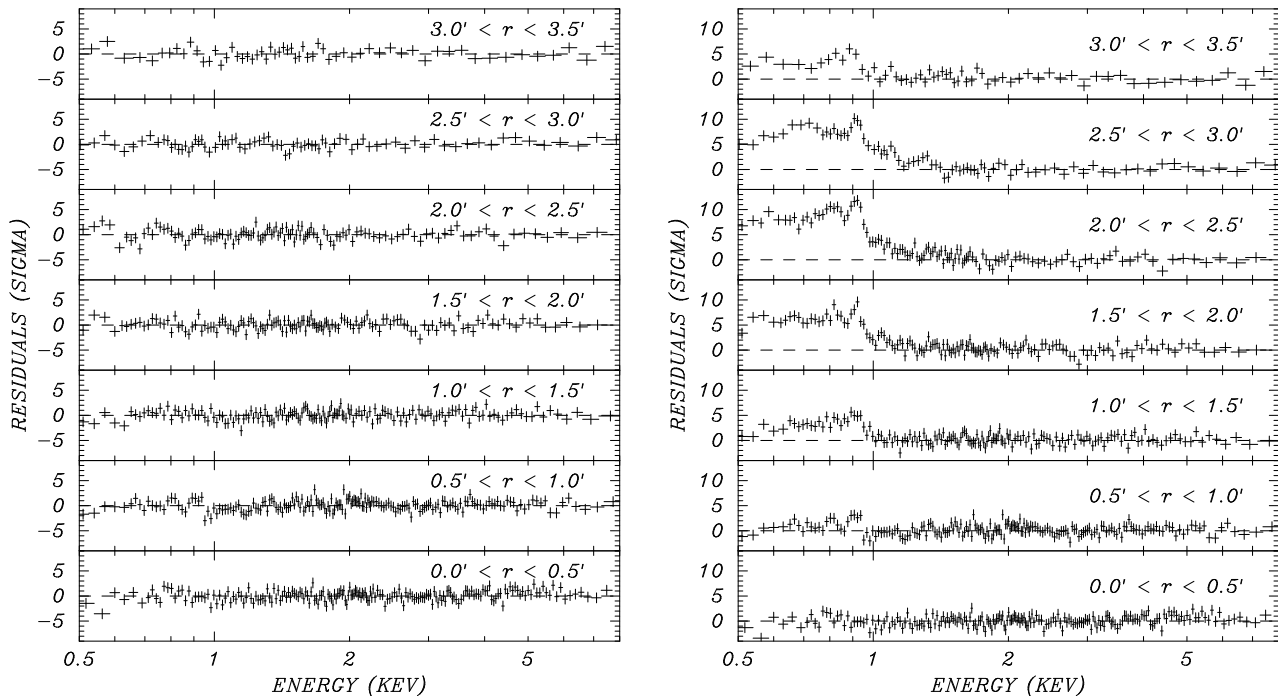


FIG. 4.— *Left Panel:* Residual from the best fit to the XMM-Newton EPIC-MOS spectrum of 3C58 in units of sigma as a function of energy. Data are accumulated in concentric annuli centered on the pulsar as defined in Table 2 and are ordered by decreasing radius (top to bottom). Each plot shows data from the combined EPIC-MOS spectrum from eight observations of the pulsar; a similar result is found for the EPIC-PN camera (not shown). The data in all cases are well-fit by a two-component power-law plus Raymond-Smith model with the parameters given in Table 2. *Right Panel:* As for adjacent panel, but with the thermal component normalization set to zero to show this contribution as a function of radius. The flux of the thermal component as a function of radius is also displayed in Figure 6.

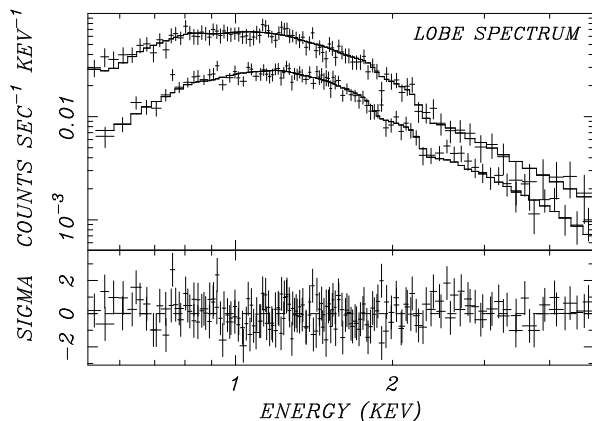


FIG. 5.— XMM-Newton EPIC spectrum of the 3C58 lobe region (see text) fitted to a power-law model. The bottom panel displays the residuals from the best fit model with  $\Gamma = 2.88 \pm 0.05$  keV.

to 0.5 – 8.0 keV. In fitting this new model, the power-law indices were fixed to the values derived at high energies. As shown in the third panel of Figure 3, however, a strong line feature at  $\sim 0.9$  keV remained unmodeled. This emission line corresponds to the He-like Ne IX transition and requires an overabundance  $\sim 3 \times [\text{Ne}/\text{Ne}_\odot]$  in the Raymond-Smith plasma model throughout the nebula.

Our final model includes a Gaussian line component to allow for the Neon emission contribution. For these fits the  $N_H$  was fixed to the value derived from the central annulus, the region with the most counts and in which

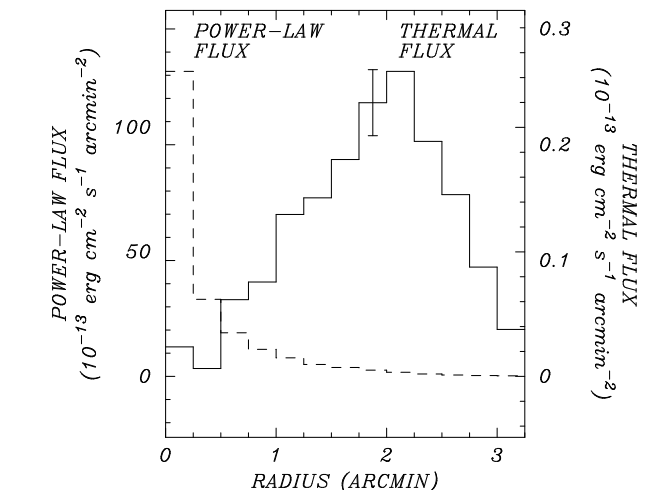


FIG. 6.— Spectroscopic detection of a thermal shell surrounding 3C58. Shown are the normalized radial profiles of the component flux from a power-law plus variable abundance Raymond-Smith plasma emission model. The observed fluxes are given in the 0.5–10.0 keV energy band using the EPIC-MOS cameras on-board XMM-Newton; a similar result is found using the EPIC-pn cameras (see Table 2). Notice the change of scale by a factor of  $\sim 500$  between the ordinate axes; less than 4% of the observed remnant flux is in the thermal component, explaining why it has proven so illusive.

the non-thermal emission strongly dominates over any thermal emission. In all cases, the final spectral fits produce an acceptable fit statistic, with the exception of the region between  $r = 2$ – $2.5'$ , and perhaps the next interior one. This can be attributed to unmodeled structure be-

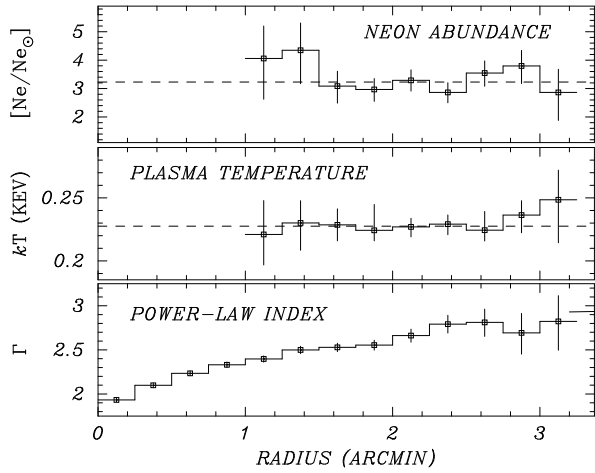


FIG. 7.— Photon index for the best fit power-law model, Raymond-Smith plasma temperature, and Ne abundance as a function of radius. The power-law index increases monotonically from  $\Gamma = 1.9$  to  $\Gamma = 2.8$ , consistent with previous reports in Torii et al. (2000) and Slane et al. (2004). The index derived from emission in the eastern lobe up to  $4'$  from the center is shown on the right axis. Both the plasma temperature and the Neon abundance show no significant radial dependence between  $1'0$  and  $3'2$

low 0.8 keV, likely additional weak thermal line emission which we lack the sensitivity to model with the current data. Table 2 gives the best fit values for the temperature and flux in each annulus after fixing the  $\Gamma$  and  $N_H$ , while Figure 4 demonstrates the dramatic change in the thermal contribution as a function of radius and the high quality of the fits in the composite model.

The overall profile of the remnant is asymmetrical, with a lobe extending to the east. In order to determine whether this is emission is powered strictly by an asymmetric relativistic wind from the pulsar (cf. Vela, Helfand et al 2001; B1509–58, Gaensler et al. 2002) or represents the breakout of the hot gas into a region of low surrounding density as is seen in some shell-type remnants, we analyzed the spectrum of the emission extracted from the lobe region defined above. Figure 5 displays the spectrum along with residuals from a power law fit which fixed the column density at the value used above for the remnant as a whole. The spectrum is well-characterized by a steep power law with index  $\Gamma = 2.88 \pm 0.06$  with no hint of any thermal emission at low energies. The spectral index is the steepest value we measured, consistent with its location farthest from the pulsar (see Figure 6).

### 3. DISCUSSION

In Figure 6, we illustrate the relative contributions of the thermal and non-thermal components as a function of radius. The thermal shell is clearly present. Note, however, that this thermal emission represents less than 4% of the observed (absorbed) flux of the remnant in the 0.5 – 10 keV band, explaining why it has proven so elusive to date. Figure 7 displays the radial dependence of the shell temperature and Neon abundance in the remnant shell – both are flat. In contrast, the power law spectral index  $\Gamma$  monotonically increases from  $\Gamma = 1.9$  at the remnant center to  $\Gamma = 2.8$  at the edge (and  $\Gamma = 2.9$  in the eastern lobe). This latter result is generally consis-

tent with earlier work (Torii et al 2000; Slane et al. 2002) although, owing to the much larger number of photons collected and the spectral-spatial decomposition we have performed, the measurements extend to a greater radius and differ in detail, remaining flat between  $2.2'$  and  $3.2'$ .

The widths of the annuli provide largely independent measurements of the spectrum at each radius given the size of the PSF. Some contamination is present from the inner, brighter rings to the outer ones, however. Since the dominant power law is flatter in the central regions, photons scattered to the outer regions bias the power law measured there. We have determined the degree of contamination from power law photons in each region by using the PSF binned in  $0.5'$  annuli and the geometrical intersection of those annuli with each extraction annulus (the minimal dependence of the PSF on photon energy allows us to ignore this complicating factor). The corrections to the measured power law slopes reported in Table 2 are modest, albeit outside the formal errors. In the central  $0.5'$  circle, the power law spectral index falls from 2.02 to 2.00, while in the first four annuli beyond this, the indices changes as follows: 2.29 becomes 2.38, 2.45 becomes 2.50, 2.55 becomes 2.58, and 2.73 becomes 2.78. Thus, the rise in spectral slope is slightly steeper than shown in Figure 7. PSF contamination effects are negligible for the thermal component since the count rate is so low.

The parameters we derive for the shell are in excellent agreement with those inferred in the early work of Bocchino et al. (2001) and with those found from a portion of the shell in the deep Chandra observation of 3C58 (Slane et al. 2004): the temperature and Neon abundance are identical at  $kT = 0.23$  keV and 3.2 solar, respectively. While these previous authors have cited the Neon overabundance as evidence that we are seeing emission from the ejecta, a growing body of work (Cunha et al. 2006 and references therein) suggests that the solar abundance of Neon has been systematically underestimated by a factor of 2.5 to 3. In that our fits do not require the statistically marginal enhancement of a factor of two in the Mg abundance reported by Slane et al. (2004), we argue that the provenance of the thermal emission remains an open question.

The total observed X-ray luminosity we derive for the shell component is  $5.9 \times 10^{32} d_{3.2}^2$  ergs  $s^{-1}$ , within the range found in Bocchino et al. (2001). This is significantly below the upper limit derived by Seward et al. (2006) for the missing Crab Nebula shell. The total mass is  $\sim 0.77 M_{\odot}$  (for a mean molecular weight of 0.6 which may not be appropriate if the bulk of the radiating material is ejecta).

Evidence has been accumulating for some time that, despite the apparently robust conclusions drawn from the historical records that 3C58 is coincident with SN1181 (Stephenson and Green 1999), the remnant properties are inconsistent with such a young age. Bietenholz (2006) provides a comprehensive summary of the arguments against an association, as well as a list of alternative scenarios. Most of the evidence suggests a remnant age of  $\sim 3000 - 5000$  years (e.g., Chevalier 2005). Our spatially resolved image of the shell adds further to the case for an age  $> 820$  yrs.

Using the X-ray emitting mass we have derived and the analytic models of PWN evolution from Chevalier (2005)

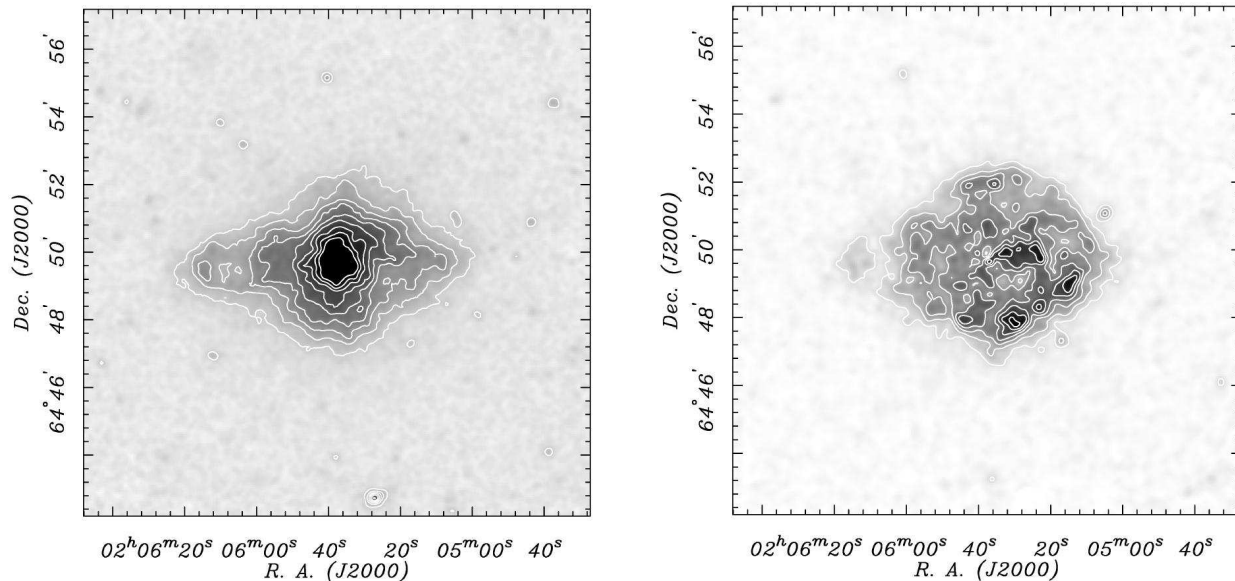


FIG. 8.— X-ray image of the pulsar wind nebula and the thermal shell in the supernova remnant 3C58. These images are the mosaic of 8 observations acquired with the *XMM-Newton* EPIC cameras. *Left*) the 1.0 – 2.0 keV exposure-corrected image with contours illustrates the morphology of the pulsar wind nebula and “lobe” regions. This image is scaled to enhance the fainter nebula emission with contours overlaid. *Right*) The same data but in the 0.5 – 1.0 keV energy band with the non-thermal contribution subtracted (see text). The intensity is scaled linearly and the seven contours are equally spaced. The symmetric, filled shell-like structure is  $\sim 5'.6$  in diameter.

we can set limits on the apparent age of the remnant. From Eq. 27 of Chevalier (2005), we can combine the observed supernova remnant radius of  $2.8 d_{3.2}$  pc and the pulsar timing-derived parameter  $\dot{E} = 2.7 \times 10^{37}$  erg  $s^{-1}$  to obtain the age  $t_3$  in units of 1000 yrs,

$$t_3 \approx 1.8 M_{ej}^{0.4} E_{51}^{-0.2}$$

where  $M_{ej}$  is the ejected mass in units of solar mass  $M_{\odot}$ . If we make the extreme assumption that all of the observed  $0.77 M_{\odot}$  of X-ray-emitting gas is ejecta, and that it represents some fraction  $\leq 1$  of the total ejected mass of the supernova, we find  $t_3 \gtrsim 1.62 E_{51}^{-0.2}$ . Thus, the pulsar must be at least twice the age of SN1181 for reasonable explosion energies and, for a more plausible ejected mass of  $\sim 5 M_{\odot}$ , the age is 3400 yrs. Alternatively, if we assume all of the observed gas has been swept up by the expanding PWN, from Chevalier’s (2005) eq. 28, we find  $t = 5100$  yrs (cf. the pulsar’s characteristic age of 5390 yrs).

The pulsar’s location with respect to the circular shell of thermal X-ray emission provides a potential test that could resolve the age controversy. The location of the pulsar is marked with a crosshair in Figure 8. It is apparent that this is not the center of the shell; a circle best matching the observed thermal emission is centered

$27'' \pm 5''$  west (and slightly north) of the pulsar’s location. For an age of 821 years, a distance of 3.2 kpc, and spherical expansion (an assumption supported by the fact we see no thermal emission in the eastern elongation of the remnant), this requires a two-dimensional pulsar velocity of  $500 d_{3.2}$  km  $s^{-1}$ . While not impossible for a young neutron star, it is worth noting that if the object has the same transverse velocity as the Crab pulsar, the remnant age would be  $3750 d_{3.2}$  yrs, consistent with other estimates. We further note that the implied trajectory for the pulsar aligns to within a few degrees of the long axis of the nebula, behavior commonly seen among PWNe. If Chandra survives for another decade, it will be possible to resolve this issue directly, as the implied proper motion of  $0.5''$  for the high-velocity scenario will be directly measurable.

This research is supported by NASA LTSA grant NAG 5-8063 to EVG and by grant SAO GO3-4026B to DJH. This research has also made use of data obtained from the High Energy Astrophysics Science Archive Research Center (HEASARC), provided by NASA’s Goddard Space Flight Center.

#### REFERENCES

- Bietenholz, M. F. 2006, ArXiv Astrophysics e-prints, arXiv:astro-ph/0603197  
 Bocchino, F., Warwick, R. S., Marty, P., Lumb, D., Becker, W., & Pigot, C. 2001, A&A, 369, 1078  
 Chevalier, R. A. 2005, ApJ, 619, 839  
 Cunha, K., Hubeny, I., & Lanz, T. 2006, ArXiv Astrophysics e-prints, arXiv:astro-ph/0606738  
 Fesen, R. A. 1983, ApJ, 270, L53  
 Gaensler, B. M., Arons, J., Kaspi, V. M., Pivovarov, M. J., Kawai, N., & Tamura, K. 2002, ApJ, 569, 878  
 Helfand, D. J., Gotthelf, E. V., & Halpern, J. P. 2001, ApJ, 556, 380  
 Jansen, F., et al. 2001, A&A, 365, L1  
 Lumb, D. H., et al. 2004, A&A, 420, 853  
 Reynolds, S. P. & Aller, H. D. 1988, ApJ, 327, 845  
 Saxton, R. D. 2003, XMM-SOC-CAL-TN-0023  
 Seward, F. D., Gorenstein, P., & Smith, R. K. 2006, ApJ, 636, 873  
 Slane, P. O., Helfand, D. J., & Murray, S. S. 2002, ApJ, 571, L45  
 Slane, P., Helfand, D. J., van der Swaluw, E., & Murray, S. S. 2004, ApJ, 616, 403  
 Stephenson, F. R., & Green, D. A. 1999, Astronomy and Geophysics, 40, 27  
 Torii, K., Slane, P. O., Kinugasa, K., Hashimoto, K., & Tsunemi, H. 2000, PASJ, 52, 875

TABLE 2  
SPECTRAL FITS AND FLUXES

Model Parameter	(0'0-0'5)	(0'5-1'0)	(1'0-1'5)	Annulus (1'5-2'0)	(2'0-2'5)	(2'5-3'0)	(3'0-3'5)
$N_{\text{H}}$ ( $10^{21}$ cm $^{-2}$ )	4.16(4.09-4.24)	4.16(fixed)	4.16(fixed)	4.16(fixed)	4.16(fixed)	4.16(fixed)	4.16(fixed)
$\Gamma$ (spectral index)	2.02(2.01-2.04)	2.29(2.27-2.31)	2.45(2.43-2.48)	2.55(2.51-2.59)	2.73(2.67-2.78)	2.81(2.70-2.92)	2.93(2.75-3.12)
PL Flux <sup>a</sup> pn	$3.43 \times 10^{-12}$	$2.80 \times 10^{-12}$	$2.06 \times 10^{-12}$	$1.50 \times 10^{-12}$	$8.40 \times 10^{-13}$	$3.86 \times 10^{-13}$	$2.05 \times 10^{-13}$
PL Flux <sup>a</sup> MOS	$4.14 \times 10^{-12}$	$3.15 \times 10^{-12}$	$2.38 \times 10^{-12}$	$1.67 \times 10^{-12}$	$9.60 \times 10^{-13}$	$4.40 \times 10^{-13}$	$2.48 \times 10^{-13}$
$\chi^2$ (DoF)	404.01(442)	207.01(251)	138.71(196)	129.18(152)	80.28 (101)	36.98(66)	39.66(52)
$kT$ (keV)	0.24(fixed)	0.24(0.20-0.29)	0.22(0.20-0.24)	0.22(0.21-0.23)	0.23(0.22-0.23)	0.23(0.22-0.24)	0.24(0.21-0.28)
Ne ( $[\text{Ne}/\text{Ne}_{\odot}]$ )	3.0(fixed)	5.5(3.0-9.4)	4.3(3.6-4.8)	3.1(2.7-3.4)	3.0(2.8-3.3)	3.6(3.2-4.0)	3.1(2.2-4.4)
$kT$ Flux <sup>a</sup> pn	...	$0.27 \times 10^{-13}$	$0.63 \times 10^{-13}$	$1.16 \times 10^{-13}$	$1.39 \times 10^{-13}$	$0.96 \times 10^{-13}$	$0.26 \times 10^{-13}$
$kT$ Flux <sup>a</sup> MOS	...	$0.18 \times 10^{-13}$	$0.57 \times 10^{-13}$	$1.16 \times 10^{-13}$	$1.63 \times 10^{-13}$	$1.05 \times 10^{-13}$	$0.26 \times 10^{-13}$
$\chi^2$ (DoF)	399.37(443)	373.58(414)	294.33(365)	345.91(319)	324.62(252)	140.76(164)	117.61(125)
Total Flux <sup>a</sup> pn	$3.43 \times 10^{-12}$	$2.82 \times 10^{-12}$	$2.12 \times 10^{-12}$	$1.62 \times 10^{-12}$	$9.76 \times 10^{-13}$	$4.79 \times 10^{-13}$	$2.34 \times 10^{-13}$
Total Flux <sup>a</sup> MOS	$4.14 \times 10^{-12}$	$3.20 \times 10^{-12}$	$2.41 \times 10^{-12}$	$1.78 \times 10^{-12}$	$1.12 \times 10^{-12}$	$5.40 \times 10^{-13}$	$2.62 \times 10^{-13}$

NOTE. — Uncertainties are 90% confidence for two interesting parameters.

<sup>a</sup>Absorbed flux in the 0.5–10 keV band in units of (ergs cm $^{-2}$  s $^{-1}$ ).Turner, M. J. L., Briel, U. G., Ferrando, P., Griffiths, R. G., &  
Villa, G. E. 2003, SPIE, 4851, 169